Active Control of Electromagnetic Fields in Layered Media

Chaoxian Qi[a], Shubin Zeng[b], Neil Jerome A. Egarguin[c], Daniel Onofrei[d] and Jiefu Chen[a]

[a]Department of Electrical and Computer Engineering, University of Houston, Houston, TX, USA; [b]CGG, Houston, TX, USA; [c]Institute of Mathematical Sciences and Physics, University of the Philippines Los Baños, Los Baños, Laguna, Philippines; [d]Department of Mathematics, University of Houston, Houston, TX, USA.

ARTICLE HISTORY
Compiled April 6, 2023

ABSTRACT
This article presents a numerical strategy for actively manipulating electromagnetic (EM) fields in layered media. The active EM field manipulation problem aims to characterize an EM source given some predetermined desired field patterns in prescribed disjoint exterior regions. The source characterization problem is treated as an inverse problem that requires solving an ill-posed optimization problem. The optimal current distribution is sought after such that the EM source can approximate the given EM fields in exterior regions. This study considers the case when the source and control regions are in a layered media, which can model various applications. Using the integral equation method, the forward operator is defined by formulating the EM fields as a function of the current at the source. The layered media Green's function (LMGF) is imposed on the integral equations to account for the effect of the layered media. We use the Rao-Wilton-Glisson (RWG) basis to get an ansatz for the necessary current on the source's surface. Hence, the integral equations are subsequently discretized and solved by the method of moments (MoM). Additionally, two regularization techniques are applied to make the approximation of ill-posed (pseudo-)inverses stable. These are the truncated singular value decomposition (TSVD) method and the Tikhonov regularization method with the Morozov Discrepancy Principle. Numerical examples demonstrate the accuracy and feasibility of the developed algorithms for the active control of the fields in layered media.

KEYWORDS
Antenna radiation pattern synthesis; electromagnetic propagation in nonhomogeneous media; integral equations; Green function; inverse problems; optimization methods.

1. Introduction

Active manipulation of electromagnetic (EM) fields addresses the problem of characterizing a current source (electric and/or magnetic) so that its radiated field approximates desired patterns in prescribed disjoint exterior regions. This problem is different from the classic inverse source problem in the sense that the patterns to be approximated are mutually different, and the source can be characterized exactly due to the analyticity of EM fields in regions without sources. The current source under control can approximate the given EM fields in specific regions. In contrast to the

CONTACT Jiefu Chen. Email: jchen84@uh.edu

forward problem of determining the radiation field of a given current source, there is no unique solution (current source) for the proposed control problem due to the existence of non-radiating currents [1,2]. The non-radiating current can be added to the source without affecting the radiated EM fields. Therefore, the active EM field control problem is solved as an ill-posed optimization problem. In recent years, the study of EM field manipulation has attracted huge attention and research efforts due to its far-reaching applications. These applications include but are not limited to, scattering cancellation or reduction (also known as cloaking) [3–11], antenna diagnostics [12–17], field synthesis or shaping (see [18–27]), etc.

Active EM field control techniques are becoming increasingly ubiquitous to enhance EM wave-based systems. Take the scattering cancellation as an example. The scattering from certain objects, such as combat aircraft, often needs to be reduced to make them invisible to radar, i.e., to reduce the objects' radar cross-section (RCS). An advanced approach for scattering cancellation is active cloaking. The active cloaking scheme seeks to suppress the dominant scattering from the object using an external source. In [4], Chen *et al.* demonstrated active scattering-cancellation cloaks in both 1-D and 3-D scenarios. The authors focused on ensuring broadband invisibility based on anomalous permittivity dispersion. Theoretically, the proposed active cloak scheme can overcome Bode–Fano bandwidth limit and operate in a much broader bandwidth than passive cloaks. In [5] (see also [6]), the authors explored active EM cloaks using the equivalence principle. External electric and/or magnetic currents are introduced to cancel out the objects' scattered fields subject to a plane wave incidence. More recently, Qian *et al.* [7] proposed an intelligent cloaking driven by the deep learning technique. The pre-trained deep neural network enables a fast response to an ever-changing incident wave and the surrounding environment without human intervention. This approach allows a wide range of real-time applications, such as moving stealth targets.

In addition, active field control techniques are also prevalent in the area of antenna diagnostics. Lopéz *et al.* [12] proposed a source reconstruction method (SRM) to establish the equivalent current distribution that radiates the same field as the actual current induced in the antenna under test (AUT). The knowledge of the equivalent currents allows the determination of the antenna radiating elements and the prediction of the AUT-radiated fields outside the equivalent currents domain. In [13], the authors formulated the source reconstruction problem on arbitrary 3-D surfaces based on integral equations. Boundary conditions for both electric and magnetic fields are applied, leading to a dual integral-equation formulation. The simulation results indicate improved accuracy of the reconstructed current. The target application is antenna diagnostics. In [16], Persson *et al.* applied the equivalent currents approach for radome diagnostics. This work reconstructs tangential EM fields from a measured far-field outside the radome surface. Using an integral representation, the measured far field is related to the equivalent surface currents on the radome surface. The proposed approach enables locating the defect area on the radome from the far-field data alone.

Moreover, active field control can be very useful in metamaterial or metasurface design. In [28], Brown *et al.* explored the possibility of metasurface design by using the electromagnetic inverse source framework. The electric and magnetic surface susceptibility profiles are computed such that the transmitted field exhibits the desired field specifications. The results show that the metasurface can focus the beam from plane waves, change the direction and radiation pattern, etc. Huang *et al.* [29] reported a reconfigurable metasurface for multifunctional control of EM waves. Recent advances in the study of the hyperbolic metamaterials, such as [30–32] also excited the search

for active control strategies for these media, such as those proposed in [33–36].

The research into new active field manipulation methods can play an important role in field synthesis applications. A particular example is field-shaping or field-focusing, which allows efficient wireless power transfer. In [20], Ayestarán *et al.* used artificial neural networks to realize near-field multi-focusing. It has the advantage of fast prediction of feeding amplitude and phase on each antenna array element. This array synthesis technique can be applied to wireless power transfer. Wireless links between the antenna array and devices are established more efficiently since power radiated at undesired positions or directions can be suppressed. Furthermore, Ayestarán *et al.* [22] introduced another array synthesis technique that can focus the near field on one or more spots and simultaneously satisfy the far-field specifications. Wu *et al.* [25] investigated the manipulation of the EM wavefront to realize the near-field power pattern control. The distributions of near-field intensities are given, and source magnitudes are also predefined. The algorithm will find the needed source phases, which can then be applied to active antenna arrays.

To the best of our knowledge, all the existing research regarding the active EM field control assumes that the surrounding medium is homogeneous or free space. Also, most works in EM control are focused on far-field control. Our work is the first one that considers the near-field active EM field control in layered media. Inspired by some particular applications, such as wireless communication between seawater and air via EM waves, wireless power transfer in subsurface formation, etc., we believe active EM control in layered media is indispensable. This article presents a unified framework and a computational platform for active EM manipulation in layered media. First, we define the forward operator by formulating the EM fields with the current source using integral equations. Note that the layered media Green's function (LMGF) is imposed on the integral equations to include the effect of layered media. Next, we consider an arbitrary 3-D closed surface as the current source, discretized using the Rao-Wilton-Glisson (RWG) basis. Accordingly, the continuous integral equations are discretized and yield a linear system that can be solved by the method of moments (MoM). Then the linear system is solved, maintaining high accuracy while requiring less power in the sense of the L^2-norm (minimum energy) [37–45]. To stabilize the ill-posed (pseudo-) inversion, we use two regularization methods, namely, the truncated singular value decomposition (TSVD) method and the Tikhonov regularization method with the Morozov Discrepancy Principle. We perform several simulations to illustrate the feasibility and accuracy of the proposed algorithm.

The rest of this article is organized as follows. Section 2 generally describes the problem and provides relevant theoretical results. Section 3 formulate the integral equation-based forward modeling. We discuss the LMGF and illustrate the MoM. In Section 4, the inversion formulation is presented. Two regularization approaches are introduced, TSVD and the Tikhonov regularization with the Morozov discrepancy principle. Section 5 shows the numerical results of the benchmark examples. Finally, we conclude the article with some remarks in Section 6.

2. Theory and formulation

This section presents a general problem statement of active EM field manipulation. We propose to cast the active EM field manipulation as an inverse problem. The main goal is to find an unknown *cause* from its known *effect* [28]. The unified framework of the inverse source problem has already been discussed in [38,39,41,45]. Though some

of those works addressed the problem of controlling the Helmholtz fields, the approach could be extended to solve the EM problems governed by Maxwell's equations. This article investigates the theoretical results controlling the EM fields in layered media. Instead of using homogenization of the medium, i.e., replacing an inhomogeneous medium with a homogeneous material with effective parameters [46], we assume that the layered medium is horizontally layered, and each layer is composed of a homogeneous material with isotropic or uniaxial (i.e., transverse isotropic) permittivity or permeability. Fig. 1 shows the simplified problem geometry. For an illustrative purpose, we consider a single source D_s, two control regions D_1, D_2 embedded in layered media. Note that the theoretical evidence in [38,40,41,45] indicates that an arbitrary number of source regions and exterior control regions can be considered in the active control scheme. The control regions D_1 and D_2 are mutually disjoint domains, i.e., $D_1 \cap D_2 = \emptyset$. We also assume that the control regions are well-separated from the source region, i.e., $(D_1 \cup D_2) \cap D_s = \emptyset$. In principle, the physical source D_s can be any arbitrary 3-D closed surface. We use a "fictitious source" D_s', which is a sphere compactly embedded in the actual source region D_s. This rids us of the complications that may be brought about by the possibly complicated shape of the EM source. Meanwhile, W_1 and W_2 that are slightly larger and mutually disjoint regions are used such that $D_1 \Subset W_1$, $D_2 \Subset W_2$, $W_1 \cap W_2 = \emptyset$ and $(W_1 \cup W_2) \cap D_s = \emptyset$. As proved in [41], accurate controls in the sense of the L^2-norm on ∂W_1 and ∂W_2 ensure smooth interior controls on ∂D_1 and ∂D_2, via regularity and uniqueness theorem for the solution of the interior Helmholtz equation. Thus, the volumetric control problem is reduced to a surface control problem.

Let us start from the EM wave propagation in a source-free layered medium in $\mathbb{R}^3$; the governing Maxwell's equations are,

$$\begin{cases} \nabla \times \mathbf{E} &= -j\omega\mu_0 \boldsymbol{\mu} \mathbf{H} \\ \nabla \times \mathbf{H} &= j\omega\varepsilon_0 \boldsymbol{\varepsilon} \mathbf{E}. \end{cases} \tag{1}$$

where $\boldsymbol{\varepsilon}$ and $\boldsymbol{\mu}$ are the complex relative permittivity and relative permeability of the planar stratified media, $\boldsymbol{\varepsilon} = \mathcal{I}_t \varepsilon_t + \hat{\mathbf{z}}\hat{\mathbf{z}}\varepsilon_z$ and $\boldsymbol{\mu} = \mathcal{I}_t \mu_t + \hat{\mathbf{z}}\hat{\mathbf{z}}\mu_z$. $\mathcal{I}_t$ is the transverse identity dyad. Note that (1) is a general formulation of Maxwell's equations in layered media, if we only consider the isotropic media, the tensors $\boldsymbol{\varepsilon}$ and $\boldsymbol{\mu}$ are reduced to scalars. The time-harmonic term $e^{j\omega t}$ is assumed but suppressed in the following

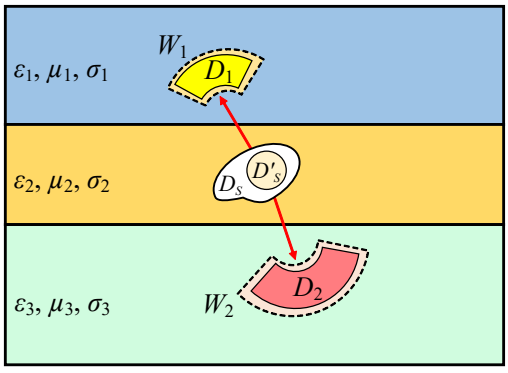

Figure 1. Problem geometry showing the control regions D_1, D_2 and the source region D_s in layered media.

demonstration.

The inverse problem addresses the source characterization from the knowledge of the field outside the source region. Finding the necessary sources that produce the given EM fields in the prescribed exterior regions is often desirable. Mathematically, the problem is to find the boundary input on the source, either surface electric current $\mathbf{J} \in \partial D_s$ or magnetic current $\mathbf{M} \in \partial D_s$ such that the solutions $(\mathbf{E}, \mathbf{H})$ of

$$\begin{cases} \nabla \times \mathbf{E} = -j\omega\mu_0 \boldsymbol{\mu} \mathbf{H} \text{ and } \nabla \times \mathbf{H} = j\omega\varepsilon_0 \boldsymbol{\varepsilon} \mathbf{E} & \text{in } \mathbb{R}^3 \setminus D_s, \\ \mathbf{E} \times \hat{\mathbf{n}} = \mathbf{M}, (\text{or } \hat{\mathbf{n}} \times \mathbf{H} = \mathbf{J}) & \text{on } \partial D_s, \\ \text{Silver-Müller radiation condition at infinity} \end{cases} \tag{2}$$

satisfy the control constraints

$$\begin{cases} \|\mathbf{E} - \mathbf{E}_j\|_{C(D_j)} \leq \delta & \text{for } j = \overline{1,2}\,, \\ \|\mathbf{H} - \mathbf{H}_j\|_{C(D_j)} \leq \delta & \text{for } j = \overline{1,2}\,, \end{cases} \tag{3}$$

where δ is the desired control accuracy threshold. In (2), $\hat{\mathbf{n}}$ is the unit exterior normal vector to ∂D_s. The Silver-Müller radiation condition in (2) at infinity is defined as [47]

$$\begin{cases} \mathbf{E}(\mathbf{x}) \times \hat{\mathbf{x}} + \frac{1}{Y}\mathbf{H}(\mathbf{x}) & = \mathcal{O}(1/|\mathbf{x}|^2)\,, \\ \mathbf{H}(\mathbf{x}) \times \hat{\mathbf{x}} - Y\mathbf{E}(\mathbf{x}) & = \mathcal{O}(1/|\mathbf{x}|^2)\,, \end{cases} \tag{4}$$

as $|\mathbf{x}| \to \infty$ uniformly with respect to $\hat{\mathbf{x}} \in \partial D_s$. The vector $\hat{\mathbf{x}} = \frac{\mathbf{x}}{|\mathbf{x}|}$ represents the unit vector pointing outside, while $Y = \sqrt{\frac{\varepsilon}{\mu}}$ is the admittance in non-conductive media. The radiation conditions force that every solution $(\mathbf{E}, \mathbf{H})$ must decay as $\frac{1}{|\mathbf{x}|}$ as $\mathbf{x} \to \infty$.

Remark 1. In [38], the authors proposed an active control strategy for acoustic fields in a two-layered ocean strategy. We believe that this can be extended to the EM paradigm through the formalism developed in [45] that employed Debeye potentials. Some preliminary numerical tests were presented in [48]. Other related works on EM control using Debeye potentials can be found in [49–53].

3. Integral equation representation

To obtain Green's function in layered media, we need to transform the time-harmonic Maxwell's equations from the spatial domain into the spectral domain by taking the 2-D Fourier transform. Physically speaking, the Fourier transformation converts a dipole source in a spatial domain into an infinite series of plane waves in the spectral domain. The modeling of plane waves propagating in layered media can be solved using the transmission line analogy [54]. First, we define the Fourier transform pair,

$$\tilde{\boldsymbol{\mathcal{F}}}(\mathbf{k}_\rho) = \int_{-\infty}^{\infty}\int_{-\infty}^{\infty} \boldsymbol{\mathcal{F}}(\boldsymbol{\rho}) e^{j\mathbf{k}_\rho \cdot \boldsymbol{\rho}} dxdy, \tag{5}$$

$$\boldsymbol{\mathcal{F}}(\boldsymbol{\rho}) = \frac{1}{(2\pi)^2} \int_{-\infty}^{\infty} \int_{-\infty}^{\infty} \tilde{\boldsymbol{\mathcal{F}}}(\mathbf{k}_\rho) e^{-j\mathbf{k}_\rho \cdot \boldsymbol{\rho}} dk_x dk_y, \tag{6}$$

where $\boldsymbol{\mathcal{F}}$ can be a scalar, vector, or dyadic quantity. Here, $\boldsymbol{\rho} = x\hat{\mathbf{x}} + y\hat{\mathbf{y}}$ is the transverse component of the position vector $\mathbf{r}$, i.e., $\mathbf{r} = \boldsymbol{\rho} + z\hat{\mathbf{z}}$. $\mathbf{k}_\rho = k_x\hat{\mathbf{x}} + k_y\hat{\mathbf{y}}$ is the transverse component of the wavenumber. Applying (5) to (1), we can obtain the spectral-domain form of Maxwell's equations,

$$\begin{cases} \tilde{\nabla} \times \tilde{\mathbf{E}} &= -j\omega\mu_0 \boldsymbol{\mu} \tilde{\mathbf{H}} \\ \tilde{\nabla} \times \tilde{\mathbf{H}} &= j\omega\varepsilon_0 \boldsymbol{\varepsilon} \tilde{\mathbf{E}}. \end{cases} \tag{7}$$

From the transmission line analogy, the transformed fields can now be written directly in terms of transformed dyadic Green's functions as,

$$\begin{aligned} \tilde{\mathbf{E}}(\mathbf{k}_\rho, z) = \int_{-\infty}^{\infty} \Big[& \tilde{\mathcal{G}}^{EJ}(\mathbf{k}_\rho, z, z') \cdot \tilde{\mathbf{J}}(\mathbf{k}_\rho, z') + \\ & \tilde{\mathcal{G}}^{EM}(\mathbf{k}_\rho, z, z') \cdot \tilde{\mathbf{M}}(\mathbf{k}_\rho, z') \Big] dz', \end{aligned} \tag{8}$$

and

$$\begin{aligned} \tilde{\mathbf{H}}(\mathbf{k}_\rho, z) = \int_{-\infty}^{\infty} \Big[& \tilde{\mathcal{G}}^{HJ}(\mathbf{k}_\rho, z, z') \cdot \tilde{\mathbf{J}}(\mathbf{k}_\rho, z') + \\ & \tilde{\mathcal{G}}^{HM}(\mathbf{k}_\rho, z, z') \cdot \tilde{\mathbf{M}}(\mathbf{k}_\rho, z') \Big] dz', \end{aligned} \tag{9}$$

where the functions, $\tilde{\mathcal{G}}^{EJ}$, $\tilde{\mathcal{G}}^{EM}$, $\tilde{\mathcal{G}}^{HJ}$, and $\tilde{\mathcal{G}}^{HM}$, in the square brackets on the right-hand side in (8) and (9) can be expressed using the analogy of transmission line voltages and currents. More detailed expressions of dyadic Green's functions in the spectral domain are elaborated in [54]. As long as we obtain the Green's function in the spectral domain, we are ready to calculate their spatial-domain forms using (6). Let us use the electric field as an example. Taking the inverse Fourier transform of (8), we can write the electric field in the spatial domain as,

$$\begin{aligned} \mathbf{E}(\mathbf{r}) = \int_{-\infty}^{\infty} \int_{-\infty}^{\infty} \int_{-\infty}^{\infty} \big[& \mathcal{G}^{EJ}(\boldsymbol{\rho} - \boldsymbol{\rho}', z, z') \cdot \mathbf{J}(\mathbf{r}') + \\ & \mathcal{G}^{EM}(\boldsymbol{\rho} - \boldsymbol{\rho}', z, z') \cdot \mathbf{M}(\mathbf{r}') \big] dx' dy' dz', \end{aligned} \tag{10}$$

where $\mathcal{G}^{EJ}$ is a dyadic tensor and it can be evaluated by

$$\begin{aligned} & \mathcal{G}^{EJ}(\boldsymbol{\rho} - \boldsymbol{\rho}', z, z') \\ & = \frac{1}{(2\pi)^2} \int_{-\infty}^{\infty} \int_{-\infty}^{\infty} \tilde{\mathcal{G}}^{EJ}(\mathbf{k}_\rho, z, z') e^{-j\mathbf{k}_\rho \cdot (\boldsymbol{\rho} - \boldsymbol{\rho}')} dk_x dk_y. \end{aligned} \tag{11}$$

Note that $\mathcal{G}^{EM}$ in (10) can be evaluated in a similar procedure. This procedure also applies to the magnetic field. To accelerate the computation of (11), we apply the Hankel transform to reduce the double integral into a single integral, i.e., the Sommerfeld integral (SI). More details can be seen in A. With a rigorous derivation, the calculation of all the components of dyadic Green's function in layered media involving general electric and magnetic sources can be expressed in terms of 16 independent SIs [55]. The detailed expressions are available in A. The evaluation of SIs in (A1) is usually carried out in the numerical sense. Some algorithms are developed for the accurate and efficient evaluation of these independent SIs, including deformed integral path [56], asymptotic singularity extraction [55,57,58], and weighted average method for integral tails [59,60].

For simplicity, we can express the integrals for evaluating $\mathbf{E}$ and $\mathbf{H}$ in the compact form:

$$\begin{aligned}\begin{bmatrix}\mathbf{E}(\mathbf{r})\\ \mathbf{H}(\mathbf{r})\end{bmatrix} &= \mathcal{K}\{\mathbf{J}(\mathbf{r}'),\mathbf{M}(\mathbf{r}')\}\\ &= \begin{bmatrix}\left\langle \boldsymbol{\mathcal{G}}^{EJ}(\mathbf{r},\mathbf{r}');\mathbf{J}(\mathbf{r}')\right\rangle + \left\langle \boldsymbol{\mathcal{G}}^{EM}(\mathbf{r},\mathbf{r}');\mathbf{M}(\mathbf{r}')\right\rangle\\ \left\langle \boldsymbol{\mathcal{G}}^{HJ}(\mathbf{r},\mathbf{r}');\mathbf{J}(\mathbf{r}')\right\rangle + \left\langle \boldsymbol{\mathcal{G}}^{HM}(\mathbf{r},\mathbf{r}');\mathbf{M}(\mathbf{r}')\right\rangle\end{bmatrix},\end{aligned} \tag{12}$$

where the notation $\langle , \rangle$ denotes the integral of products of two functions separated by the comma over their common spatial support, with a dot over the comma indicating a dot product. To perform the integrals numerically, MoM is applied to reduce the continuous integrals to discrete EM moments. This is realized by discretizing the source surface ∂D_s into finite triangle patches such that the surface currents can be expressed as

$$\begin{cases}\mathbf{J}(\mathbf{r}') &= \sum\limits_{n=1}^{N} I_n^S \boldsymbol{\Lambda}_n(\mathbf{r}'),\\ \mathbf{M}(\mathbf{r}') &= \sum\limits_{n=1}^{N} V_n^S \boldsymbol{\Lambda}_n(\mathbf{r}'), \quad \mathbf{r}' \in \partial D_s,\end{cases} \tag{13}$$

where N is the total number of basis functions. $\mathbf{I}^S = \begin{bmatrix} I_1^S & I_2^S & \cdots & I_N^S \end{bmatrix}$ and $\mathbf{V}^S = \begin{bmatrix} V_1^S & V_2^S & \cdots & V_N^S \end{bmatrix}$ are two vectors whose elements are the coefficients of discredited surface currents $\mathbf{J}$ and $\mathbf{M}$. Each $\boldsymbol{\Lambda}_n$ is a divergence-conforming Rao-Wilton-Glisson (RWG) basis function [61].

4. Inversion

In Section 3, the integral equation method is used to define the forward operator. Once the electric and magnetic currents are given, the EM fields can be evaluated via the forward operator $\mathcal{K}$ in (12). We can express the forward modeling in a compact form $\mathcal{K}(\mathbf{J},\mathbf{M}) = (\mathbf{E},\mathbf{H})$. In contrast to the forward problem of determining the radiation field of a given current source, the electromagnetic inverse source problem aims to find an unknown *cause* from its known *effect* [28], i.e., $(\mathbf{J},\mathbf{M}) = \mathcal{K}^{-1}(\mathbf{E},\mathbf{H})$. Following the same strategy in [38,39,41–43,45], the continuous integral operator $\mathcal{K}$ is converted into matrix form by discretizing the control regions and source region into discrete meshes.

Then the forward operator $\mathcal{K}$ yields a linear system,

$$\mathbf{A}\mathbf{w}_d = \mathbf{b}, \tag{14}$$

where $\mathbf{w}_d = [\mathbf{I}^S; \mathbf{V}^S]$ is a vector containing the coefficients in discrete forms of $(\mathbf{J}, \mathbf{M})$ in (13). $\mathbf{A}$ represents the matrix of moments computed from the propagator $\mathcal{K}$, and $\mathbf{b}$ is the vector of $(\mathbf{E}, \mathbf{H})$ at the mesh of evaluation points distributed within the control regions. In (14), $\mathbf{w}_d$ is to be determined from the knowledge of the discrete EM fields, i.e., $\mathbf{b}$. In principle, $\mathbf{w}_d$ can be evaluated by $\mathbf{w}_d = \mathbf{A}^{-1}\mathbf{b}$. However, $\mathbf{A}$ is not square in most cases due to the inconsistent dimension of $\mathbf{w}_d$ and $\mathbf{b}$. Consequently, $\mathbf{A}^{-1}$ does not exist. The alternative way is to find a solution $\mathbf{w'}_d$ that can produce the approximate field $\mathbf{b}'$. Note that the data misfit can determine the proximity. Therefore, we can formulate an optimization problem

$$\hat{\mathbf{w}}_d = \underset{\mathbf{w}_d \in \partial D_s}{\arg\min} \left[\sum_{j=1}^{2} \xi_j \|\mathbf{A}_j \mathbf{w}_d - \mathbf{b}_j\|^2_{L^2(\partial W_j)} \right], \tag{15}$$

where ξ_j is the weight to balance the importance of the residuals, $j = \overline{1,2}$. Solving the optimization problem (15) yields a classical least-squares inversion. The minimization of the discrete least-squares cost functional can ultimately result in an ill-posed linear system, i.e., there is no unique solution. Hence, the original problem (15) must be regularized. We can apply two commonly used regularization approaches, including the truncated singular value decomposition (TSVD) and the Tikhonov regularization with the Morozov discrepancy principle [62,63]. The TSVD method is modified from the SVD method. TSVD has the virtues of being straightforward to implement and it allows getting a quick estimate on the degree of ill-posedness by examining the singular values. The drawback of TSVD is its computational cost, caused by performing the necessary matrix decomposition. Tikhonov regularization is typically the method of first choice for linear problems. The generalized Tikhonov regularization provides an opportunity to incorporate known properties of the solution into the solution method [62]. Compared with the TSVD method, Tikhonov regularization does not suffer from the expensive computational cost. However, classic question arises, "How to choose the regularization parameter?" In the following, we first formulate the inversion with these two regularization methods and then we will compare the inversion performance against each other.

We start from the TSVD regularization. We know from matrix algebra that any matrix $\mathbf{A} \in \mathbb{R}^{m \times n}$ can be written in the form,

$$\mathbf{A} = \mathbf{U}\mathbf{D}\mathbf{V}^\intercal \tag{16}$$

where the superscript 'T' represents the matrix transpose. Let $\mathbf{U} \in \mathbb{R}^{m \times m}$ and $\mathbf{V} \in \mathbb{R}^{n \times n}$ be the orthogonal matrices satisfying $\mathbf{U}^\intercal\mathbf{U} = \mathbf{U}\mathbf{U}^\intercal = \mathbf{I}$, and $\mathbf{V}^\intercal\mathbf{V} = \mathbf{V}\mathbf{V}^\intercal = \mathbf{I}$. $\mathbf{I}$ is the identity matrix while $\mathbf{D} \in \mathbb{R}^{m \times n}$ is a diagonal matrix whose diagonal elements d_j are the singular values of $\mathbf{A}$. The minimum norm solution of the equation $\mathbf{A}\mathbf{x} = \mathbf{b}$ is given by $\mathbf{x} = \mathbf{V}\mathbf{D}^-\mathbf{U}^\intercal\mathbf{b}$, where $\mathbf{V}\mathbf{D}^-\mathbf{U}^\intercal$ is the pseudo-inverse of $\mathbf{A}$. $\mathbf{D}^-$ is a diagonal matrix with diagonal elements ${d_j}^{-1}$. The numerical instability issue may occur when the r^{th} diagonal element d_r in $\mathbf{D}$ is much smaller than d_1 , i.e., ${d_r}^{-1}$ appearing in $\mathbf{D}^-$ is much larger than ${d_1}^{-1}$. $\mathbf{D}^-$ then suffers from bad conditioning. To tackle this problem, we need to ignore the small diagonal elements which are below a defined

threshold. This is the truncated SVD (TSVD) method. Hence, the TSVD solution is expressed as

$$\hat{\mathbf{w}}_d = \mathbf{V}\mathbf{D}_t^{-}\mathbf{U}^{\intercal}\mathbf{b}, \tag{17}$$

where t denotes the number of diagonal elements in the truncated matrix.

Compared with (15), the Tikhonov regularization method introduces a regularization parameter as a penalty weight for the power required by the solution

$$\hat{\mathbf{w}}_d = \underset{\mathbf{w}_d \in \partial D_s}{\arg\min} \left[\sum_{j=1}^{2} \xi_j \|\mathbf{A}_j \mathbf{w}_d - \mathbf{b}_j\|^2_{L^2(\partial W_j)} + \alpha \|\mathbf{w}_d\|^2_{L^2(\partial D_s')} \right], \tag{18}$$

where $\alpha > 0$ is the regularization parameter. The Tikhonov regularization can be regarded as a balance between two requirements, i.e.,

(1) $\hat{\mathbf{w}}_d$ should give a small residual $\mathbf{A}\mathbf{w}_d - \mathbf{b}$
(2) $\hat{\mathbf{w}}_d$ should be small in the sense of L^2-norm.

The regularization parameter α is selected to minimize the misfit. $\hat{\mathbf{w}}_d$ is considered to be an acceptable characterization if $\|\mathbf{A}\mathbf{w}_d - \mathbf{b}\| \leq \delta$, where δ is a desired accuracy threshold. The optimal α is determined by the Morozov's discrepancy principle [62,63]. The idea of Morozov's discrepancy principle is to choose $\alpha > 0$ such that $\|\mathbf{A}\mathbf{w}_d - \mathbf{b}\| = \delta$. $\mathbf{w}_d$ is then taken to be the Tikhonov solution with α determined by Morozov's discrepancy principle,

$$\hat{\mathbf{w}}_d = (\alpha \mathbf{I} + \mathbf{A}^* \mathbf{A})^{-1} \mathbf{A}^* \mathbf{b}, \tag{19}$$

where $\mathbf{A}^*$ is the complex conjugate transpose of $\mathbf{A}$.

To summarize, two regularization methods, including TSVD and Tikhonov regularization, are introduced in this section. Combined with the forward modeling in Section 3, the inverse source problem can be tackled in two approaches, of which the algorithms can be summarized as Algorithm 1 and Algorithm 2.

5. Numerical results

To validate the feasibility of proposed algorithms, we present several numerical simulations in this section. For an illustrative purpose, we consider a three-layer medium as shown in Fig. 2. First, we investigate the EM fields control in one near region in Fig. 2(a). Then, we extend our numerical study into a multiple-region regime with two near field control regions W_1 and W_2 as sketched in Fig. 2(b). The control regions and the source are placed in different layers. Note that the control region can be in the same layer as the source. In general, the physical source D_s can have an arbitrary shape as long as it has a Lipschitz boundary, which compactly includes the fictitious source D_s' and is well separated from the control regions.

5.1. One region control

We start from a simple geometry where only one control region and one source are considered. The background medium is horizontally layered transverse isotropic. From

Algorithm 1: TSVD Regularization

input : Prescribed fields, $(\mathbf{E}_j, \mathbf{H}_j)$ in D_j, $j = \overline{1,2}$, accuracy threshold δ.

$(\mathbf{I}^S, \mathbf{V}^S) \leftarrow (\mathbf{J}, \mathbf{M})$ using (13),

$\mathbf{b}_j \leftarrow (\mathbf{E}_j, \mathbf{H}_j)$,

$\mathbf{b} = [\mathbf{b}_1; \mathbf{b}_2]$,

for $n = 1$ **to** N **do**

  Compute $\boldsymbol{\mathcal{G}}_n^{EJ}$, $\boldsymbol{\mathcal{G}}_n^{EM}$, $\boldsymbol{\mathcal{G}}_n^{HJ}$, $\boldsymbol{\mathcal{G}}_n^{HM}$ via (A2)-(A5),

end

$\mathbf{A}_j = \begin{bmatrix} \boldsymbol{\mathcal{G}}^{EJ}, \boldsymbol{\mathcal{G}}^{EM} \\ \boldsymbol{\mathcal{G}}^{HJ}, \boldsymbol{\mathcal{G}}^{HM} \end{bmatrix}$,

$\mathbf{A} = [\mathbf{A}_1; \mathbf{A}_2]$,

$\mathbf{A} = \mathbf{U}\mathbf{D}\mathbf{V}^\intercal$, $\mathbf{D}^- = pinv(\mathbf{D})$,

$t \leftarrow 1000$, truncate the first 1000 singular values,

$\mathbf{w}_d = \mathbf{V}\mathbf{D}_t^-\mathbf{U}^\intercal\mathbf{b}$,

$\tau^2 = \left[\sum_{j=1}^{2} \xi_j \|\mathbf{A}_j\mathbf{w}_d - \mathbf{b}_j\|^2\right]$,

while $\tau^2 > \delta^2$ **do**

  $t \leftarrow (t + 100)$,

  $\mathbf{w}_d = \mathbf{V}\mathbf{D}_t^-\mathbf{U}^\intercal\mathbf{b}$,

  $\tau^2 = \left[\sum_{j=1}^{2} \xi_j \|\mathbf{A}_j\mathbf{w}_d - \mathbf{b}_j\|^2\right]$.

end

$(\mathbf{I}^S, \mathbf{V}^S) \leftarrow \mathbf{w}_d$,

$(\mathbf{J}, \mathbf{M}) \leftarrow (\mathbf{I}^S, \mathbf{V}^S)$,

output: Surface currents $\mathbf{J}$ and/or $\mathbf{M} \in D_s$.

Algorithm 2: Tikhonov Regularization

input : Prescribed fields, $(\mathbf{E}_j, \mathbf{H}_j)$ in D_j, $j = \overline{1,2}$, accuracy threshold δ.

$(\mathbf{I}^S, \mathbf{V}^S) \leftarrow (\mathbf{J}, \mathbf{M})$ using (13),

$\mathbf{b}_j \leftarrow (\mathbf{E}_j, \mathbf{H}_j)$,

$\mathbf{b} = [\mathbf{b}_1; \mathbf{b}_2]$,

for $n = 1$ **to** N **do**

  Compute $\boldsymbol{\mathcal{G}}_n^{EJ}$, $\boldsymbol{\mathcal{G}}_n^{EM}$, $\boldsymbol{\mathcal{G}}_n^{HJ}$, $\boldsymbol{\mathcal{G}}_n^{HM}$ via (A2)-(A5),

end

$\mathbf{A}_j \leftarrow \begin{bmatrix} \boldsymbol{\mathcal{G}}^{EJ}, \boldsymbol{\mathcal{G}}^{EM} \\ \boldsymbol{\mathcal{G}}^{HJ}, \boldsymbol{\mathcal{G}}^{HM} \end{bmatrix}$,

$\mathbf{A} = [\mathbf{A}_1; \mathbf{A}_2]$,

$\alpha \leftarrow 10^{-12}$,

$\beta \leftarrow 1.05$,

$\mathbf{w}_d = (\alpha \mathbf{I} + \mathbf{A}^* \mathbf{A})^{-1} \mathbf{A}^* \mathbf{b}$,

$\tau^2 = \left[\sum_{j=1}^{2} \xi_j \|\mathbf{A}_j \mathbf{w}_d - \mathbf{b}_j\|^2 + \alpha \|\mathbf{w}_d\|^2 \right]$,

while $\tau^2 > \delta^2$ **do**

  $\alpha \leftarrow \dfrac{\alpha}{\beta}$,

  $\mathbf{w}_d = (\alpha \mathbf{I} + \mathbf{A}^* \mathbf{A})^{-1} \mathbf{A}^* \mathbf{b}$,

  $\tau^2 = \left[\sum_{j=1}^{2} \xi_j \|\mathbf{A}_j \mathbf{w}_d - \mathbf{b}_j\|^2 + \alpha \|\mathbf{w}_d\|^2 \right]$,

end

$(\mathbf{I}^S, \mathbf{V}^S) \leftarrow \mathbf{w}_d$,

$(\mathbf{J}, \mathbf{M}) \leftarrow (\mathbf{I}^S, \mathbf{V}^S)$,

output: Surface currents $\mathbf{J}$ and/or $\mathbf{M} \in D_s$.

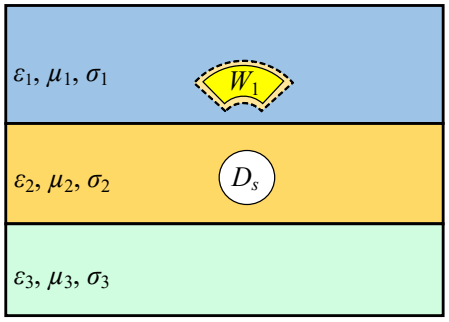

(a)

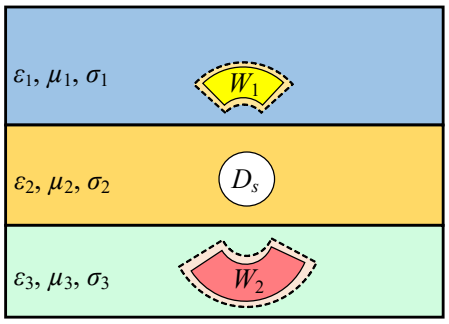

(b)

Figure 2. Problem geometry: control region(s) W_1, W_2, and the source region D_s in layered media. (a) One control region. (b) Two control regions.

the top to bottom, the relative permittivity ε_r is $[1, 2, 1]$. The conductivity is zero, i.e., the media is lossless. The layered media is non-magnetic, i.e., $\mu_r = 1$. The control region is an annular sector and satisfies $D_1 \Subset W_1$, where W_1 is defined in the spherical coordinates (with respect to the origin) by

$$\begin{aligned} W_1 = \Big\{ (r, \theta, \phi) : r \in [0.5, 0.55], \theta \in \Big[-\frac{\pi}{4}, \frac{\pi}{4} \Big], \\ \phi \in \Big[\frac{3\pi}{4}, \frac{5\pi}{4} \Big] \Big\} + [0.3, 0, 0]. \end{aligned} \tag{20}$$

It should be noted that the spherical coordinate allows a simpler representation of W_1. When we calculate the Green's functions involving the observation and source points, we convert the spherical mesh coordinates on the annular sector to Cartesian coordinates. In our experiment, the operating frequency is 47.7 MHz. Throughout this subsection, we use a sphere as the source D_s, and its radius is 0.31 m centered at the origin. We assume that only electric current $\mathbf{J}$ is present on D_s. In our experiment, we apply the RWG basis functions to discretize the source surface. We used 2808 triangle patches and the number of unknowns, i.e., degrees of freedom (DoF) is 4212. The prescribed field in W_1 is a plane wave and the electric field is defined by $\mathbf{E}(x, y, z) = \hat{\mathbf{x}}\mathbf{E}_0 \cdot e^{-jkz}$, where $k = 1$ is the wavenumber in the top layer. The magnetic field can be attained by $\mathbf{H}(\mathbf{r}) = \dfrac{1}{\omega\mu}\hat{\mathbf{z}} \times \mathbf{E}(\mathbf{r})$. The defined electric field in Cartesian coordinates indicates the EM wave propagates along the $\hat{\mathbf{z}}$ direction, and the electric field is polarized in the $\hat{\mathbf{x}}$ direction. On the boundary of the control region, there are 2750 mesh points. Since we are combining 6 components of EM fields together, the number of mesh points should be limited, otherwise the system is too large.

Two approaches were used to address the inverse problem, namely, the "integral equation- TSVD" and the "integral equation-Tikhonov" methods. We shall compare the performance of these two methods. Here and in the following content, we use the L^2-norm error to measure the control performance, which is defined as

$$\|err\|_{L^2(\partial W_j)} = \begin{cases} \frac{\|\mathbf{G}_j - \mathbf{P}_j\|_{L^2(\partial W_j)}}{\|\mathbf{P}_j\|_{L^2(\partial W_j)}} & \text{if } \|\mathbf{P}_j\|_{L^2(\partial W_j)} \neq 0, \\ \|\mathbf{G}_j - \mathbf{P}_j\|_{L^2(\partial W_j)} & \text{if } \|\mathbf{P}_j\|_{L^2(\partial W_j)} = 0, \end{cases} \tag{21}$$

for each $j = \overline{1, 2}$. $\mathbf{G}_j = \mathbf{A}_j \mathbf{w_d}$ denotes the generated field, and $\mathbf{P}_j$ is prescribed field. $\mathbf{G}_j$ and $\mathbf{P}_j$ can be either $\mathbf{E}$ or $\mathbf{H}$. Such a L^2-norm error is an overall quantitative measure of control performance. Additionally, we define another measure to show the control accuracy in each mesh point, i.e., the pointwise error,

$$err_i = \begin{cases} \frac{|G_i - P_i|}{|P_i|} & \text{if } P_i \neq 0, \\ |G_i - P_i| & \text{if } P_i = 0, \end{cases} \tag{22}$$

where err_i is the relative or absolute error in the i^{th} evaluation point. In what follows, we present the simulation results of the one-region control. Fig. 3 shows the $\mathbf{E}$ and $\mathbf{H}$ obtained by the "integral equation- TSVD" method. Only non-zero components $\mathbf{E}_x$ and $\mathbf{H}_y$ are displayed. In Fig. 3, the first row shows the $\mathbf{E}_x$ synthesis, and the second row is $\mathbf{H}_y$. Three columns represent the prescribed field, generated field, and pointwise relative error, respectively. Note that only the real part of the fields is shown here since

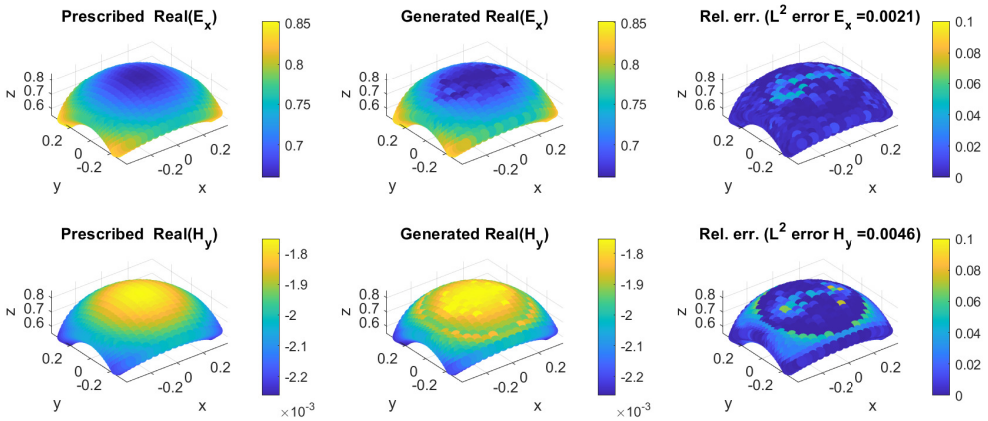

Figure 3. Electric and magnetic field synthesis in an exterior control region by "integral equation-TSVD" method.

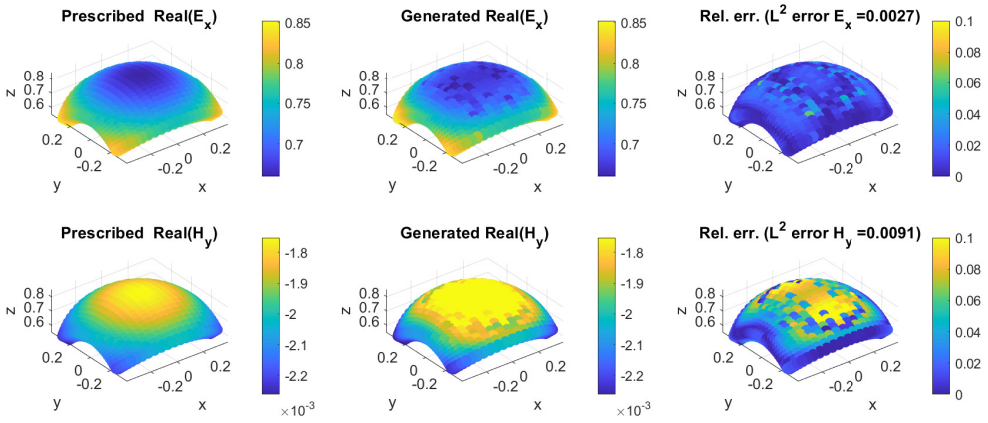

Figure 4. Electric and magnetic field synthesis in an exterior control region by "integral equation-Tikhonov" method.

the imaginary part exhibits similar results. We notice that the generated fields, either electric or magnetic, almost have the same pattern as the prescribed fields. Though some artifacts are observed in the generated fields, the maximum relative error of the approximated fields is less than 0.1. The overall L^2-norm error is within the order 10^{-3}. Similarly, we perform the experiment using the "integral equation-Tikhonov" method. Fig. 4 demonstrates the control performance. We notice the approximated $\mathbf{E}_x$ is almost the same as that in Fig. 3. However, the generated $\mathbf{H}_y$ in Fig. 4 is worse than the "integral equation-TSVD" method. The pointwise relative error exceeds 0.1.

The characterized current is shown in Fig. 5, where Fig. 5(a) and Fig. 5(b) correspond the results of the "integral equation-TSVD" method and "integral equation-Tikhonov" method. Due to the wide range of the current magnitude on D_s, we make use of the logarithmic scale of current density, i.e., $\mathrm{dB\,A\,m^{-2}}$. We observe that the inverted current has an irregular distribution, and its amplitude is considerable in some areas. The characterized current source is a high-power source for both approaches.

From the accuracy perspective, the TSVD regularization is better than the Tikhonov regularization. Essentially, the Tikhonov regularized solution is the same as the SVD

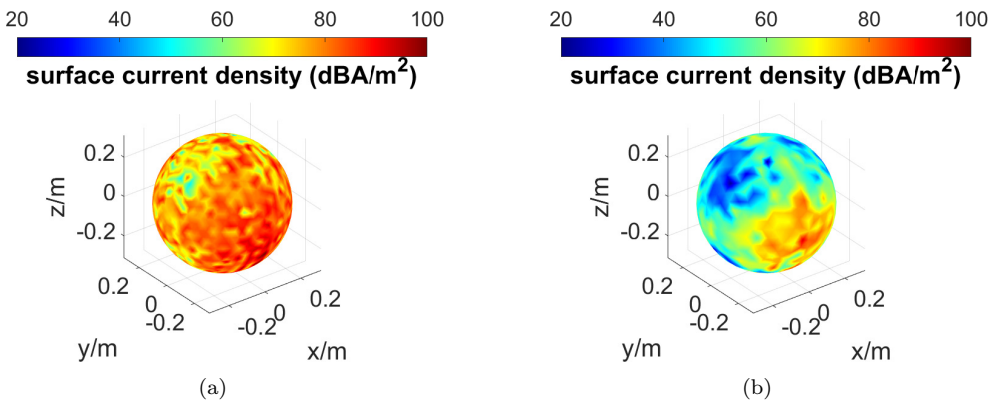

Figure 5. Characterized surface electric current (**J**) on the source ∂D_s. (a) "integral equation-TSVD" method. (b) "integral equation-Tikhonov" method.

solution as long as the regularization parameter α is sufficiently small (smaller than the smallest singular value) [62]. However, the selection of an appropriate regularization parameter α in (18) depends on the step size β in Algorithm 2. The number of iterations will be large if β is too small. Consequently, the computational cost would increase. In contrast, the optimal α could be missed if the step size is too large. However, this limitation does not exist in the TSVD method. In terms of the characterized current source, the current obtained by the "integral equation-TSVD" method is about 20 dB larger than the "integral equation-Tikhonov" method. In this regard, the current source is more likely to be implemented if we use the Tikhonov regularization, which allows lower power consumption.

Remark 2. Note that the Tikhonov approach addresses the minimum energy solution (with $\|\|_{L^2}$), while the TSVD approach does not. That is why the two solutions appear differently in Fig. 5.

5.2. Two region control

In this subsection, EM field control in two regions is investigated. We examine the performance of our framework in creating a plane EM wave in W_1 and null field in W_2. This technique could be potentially used for wireless power transfer or EM contrast control, where the EM wave is projected in the target areas. Whereas the power radiated in undesired regions is suppressed. The problem geometry is shown in Fig. 2(b), where W_1, D_s, and W_2 locate in three layers from top to bottom. The background medium is identical to the previous example. W_1 and W_2 are defined in the spherical coordinate,

$$\begin{aligned} W_1 = \Big\{ (r,\theta,\phi) : r \in [0.5, 0.55], \theta \in \Big[-\frac{\pi}{8}, \frac{\pi}{8}\Big], \\ \phi \in \Big[\frac{3\pi}{4}, \frac{5\pi}{4}\Big] \Big\} + [0.1, 0, 0], \end{aligned} \tag{23}$$

$$W_2 = \left\{ (r,\theta,\phi) : r \in [0.35, 0.4], \theta \in \left[\frac{7\pi}{8}, \frac{9\pi}{8}\right], \right. \\ \left. \phi \in \left[\frac{3\pi}{4}, \frac{5\pi}{4}\right] \right\} - [0.4, \pi, 0]. \tag{24}$$

In W_1, the radiating field is a plane EM wave propagating in the $\hat{\mathbf{z}}$ direction. The electric field is polarized in the $\hat{\mathbf{x}}$ direction, i.e., only $\mathbf{E}_x$ is non-zero. As a result, the magnetic field only has the $\mathbf{H}_y$ component. The prescribed field in W_2 is null. The surface current is characterized using the proposed two approaches. The number of DoFs is the same as that in Subsection 5.1, i.e., 4212. While the number of mesh points (3960) on the control regions is larger than the one-region regime since more points are required to increase the resolution. This is also due to the challenge posed by contrast control. Then we could calculate the radiated field by the current source via the forward operator $\mathcal{K}$. The simulation results are shown in Fig. 6 for "integral equation-TSVD" method and Fig. 7 for "integral equation-Tikhonov" method. In each figure, the first two rows respectively denote $\mathbf{E}$ and $\mathbf{H}$ in W_1, the third row is the absolute $\mathbf{E}$ and $\mathbf{H}$ in W_1. In particular, the three columns in the first two rows are the prescribed field, generated field, and the pointwise relative error. We observe that the generated $\mathbf{E}$ and $\mathbf{H}$ fields are in good agreement with the prescribed fields in both Fig. 6 and Fig. 7. The maximum pointwise relative errors are less than 5%. The overall L^2-norm errors are within 10^{-3}, especially, it is in order of 10^{-4} for $\mathbf{E}_x$ in Fig. 6.

Regarding the control performance in W_2, the generated fields could be regarded as the absolute error since the prescribed fields are zero. In the third row of Fig. 6, the generated $\mathbf{E}$ is in order 10^{-3} and $\mathbf{H}$ is in order 10^{-6}. Compared with the $\mathbf{E}$ in W_1, the magnitude is almost three orders lower in W_2, which also applies to $\mathbf{H}$. Namely, the power in W_1 is about 60 dB lower than that in W_2. In this regard, the EM contrast control is realized. The power is projected in W_1 while the radiated power in W_2 is suppressed. The characterized currents are shown in Fig. 8. The first subplot is obtained by the "integral equation-TSVD" method, while the second one shows the results of the "integral equation-Tikhonov" method. We find the magnitudes of both currents are enormous, indicating high-power sources. Unlike the one-region regime, the current distributions are very similar by the proposed methods. This observation can back up the statement that the Tikhonov regularized solution is essentially the same as the TSVD solution as long as the regularization parameter α is sufficiently small.

Remark 3. In Subsection 5.2, we showed the contrast control where a plane wave is approximated in one region while the null field is realized in the other one. In general, more control regions could be added so that the radiated field is forced to approximate more and more different patterns in all these regions, which is far from a true inverse source problem scenario where one measured field data in the control regions belonging to an EM field interacting with the measurement apparatus.

6. Conclusion

This article presents a unified framework for actively manipulating electromagnetic fields in layered media. We cast the EM field manipulation as an inverse source problem where the main goal is to characterize the current source from the knowledge of the radiated field outside the source region. Firstly, we formulate the EM fields re-

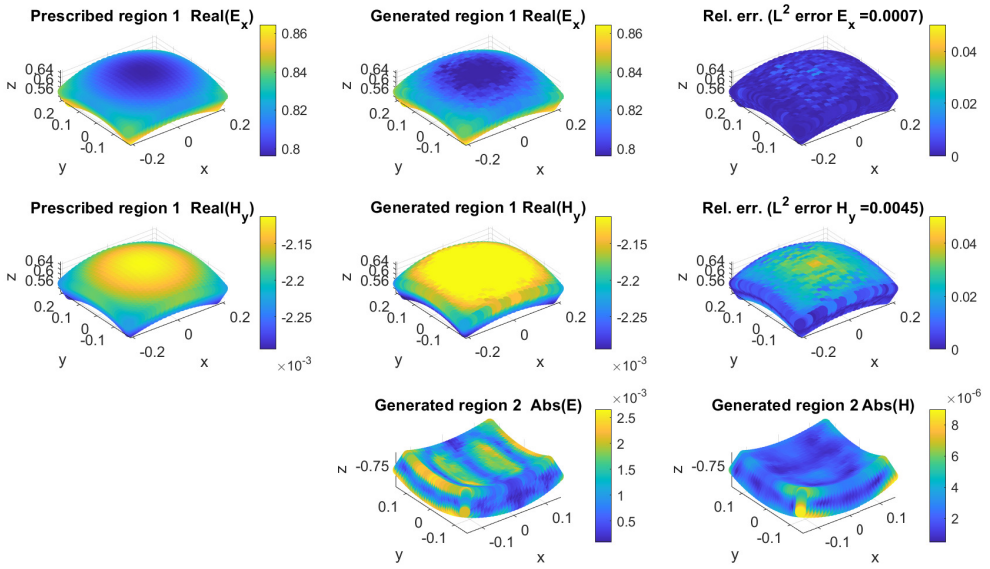

Figure 6. Electric and magnetic field synthesis in two exterior control regions by the "integral equation-TSVD" method.

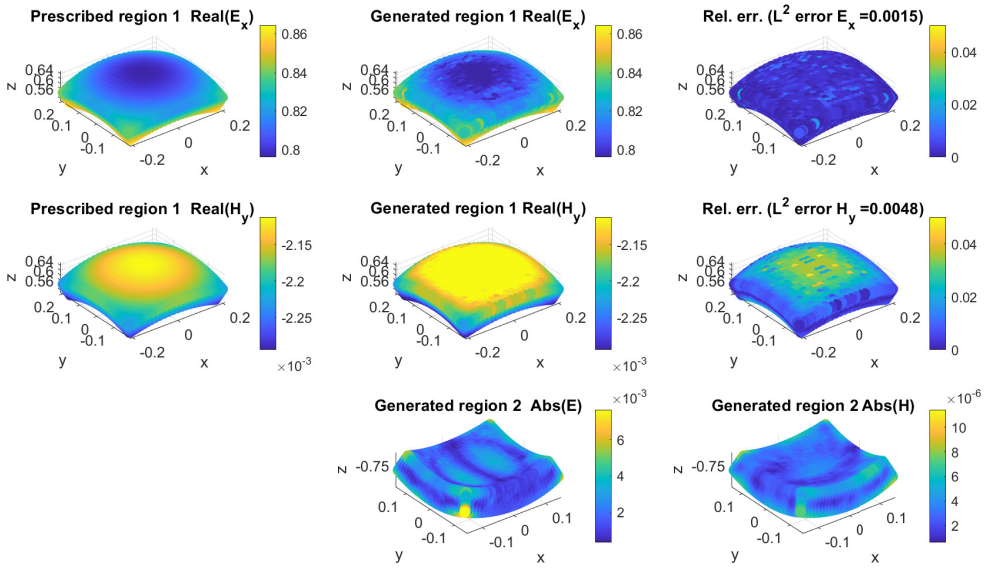

Figure 7. Electric and magnetic field synthesis in two exterior control regions by "integral equation-Tikhonov" method.

garding the current source using the integral equation method. We impose the dyadic Green's function in layered media on the integral equations to account for multiple reflections in the background medium. The source region and the control region are discretized to dense enough meshes of points. Thus, the integral equation is reduced to a discrete linear system by the method of moment. The linear system is solved in

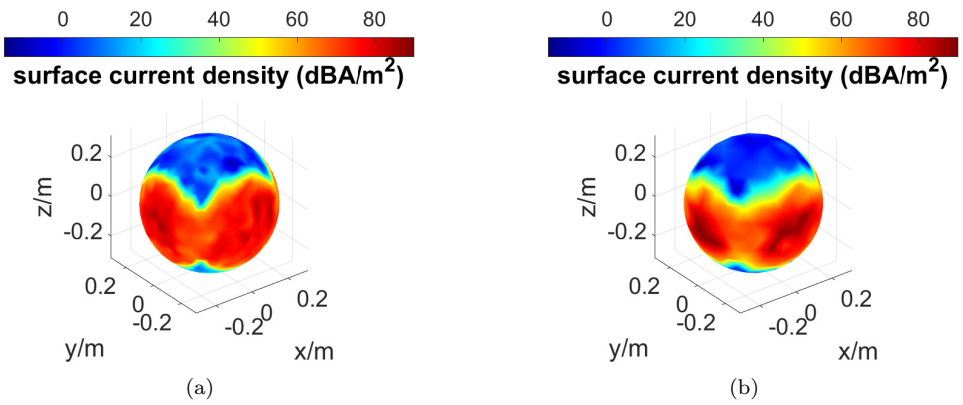

Figure 8. Characterized surface electric current (**J**) on the source ∂D_s to control EM fields in two regions. (a) "integral equation-TSVD" method. (b) "integral equation-Tikhonov" method.

the sense of the minimum L^2-norm (least-squares inversion) as directly solving the linear system would result in unstable solutions due to the ill-posedness of the inverse problem. We use the regularization methods to stabilize the solution to the inversion, namely the truncated singular value decomposition (TSVD) method and the Tikhonov regularization method.

Two simulations are provided to support the proposed algorithms. The first example contains one control region and one source region. The second example has two control regions and one source. We place the control region(s) and the source in the planar stratified media in both examples. The simulation results demonstrate the existence of a current source (modeled as surface electric current). It is capable of approximating *a priori* given fields in some near control regions. In addition, we compare the control performance between two approaches, i.e., the "integral equation-TSVD" method and the "integral equation-Tikhonov" method. In the one-region scenario, the "integral equation-TSVD" method outperforms the other method in control accuracy. However, the characterized current source by the "integral equation-TSVD" method requires higher power. The high-power source is a limitation when the source is physically implemented. The second simulation illustrates the capability of achieving the EM contrast control by our methods. Two regions are prescribed to be a plane EM wave and null. The contrast control can facilitate focusing applications such as wireless power transfer, beamforming, etc. We observe that the calculated current source can produce the EM field with small misfits between the given EM fields in control regions. Unlike the first simulation, the control accuracies evaluated by the pointwise error and L^2-norm error of the two approaches are almost identical. Both two approaches show that the L^2-norm error is within an order of 10^{-3}. Meanwhile, the current sources have a very similar distribution as the Tikhonov regularized solution is essentially the same as the TSVD solution as long as the regularization parameter α is sufficiently small.

In general, the current source can be modeled as an electric and/or magnetic current. The background medium can have an arbitrary number of layers, and each layer can be either isotropic or anisotropic. In addition, the number of source regions and control regions is also arbitrary as long as each region is well-separated from the others, i.e., with no overlapping. Otherwise, Green's function can be highly singular. In this article, we consider a simplified three-layer medium. The simulation results indicate that our approaches can manipulate the EM fields in layered media. The relative error of the

control could be as low as 10^{-3}.

Acknowledgement

J. Chen and C. Qi would like to acknowledge the National Science Foundation, USA for funding their work under the award 1801925. D. Onofrei and N. J. A. Egarguin would like to acknowledge the Army Research Office, USA, for funding their work under the award W911NF-17-1-0478.

Disclosure statement

The authors do not have any conflict of interest.

References

[1] Quijano JLA, Vecchi G. Field and source equivalence in source reconstruction on 3d surfaces. Progress In Electromagnetics Research. 2010;103:67–100.

[2] Mohajer M, Safavi-Naeini S, Chaudhuri SK. Surface current source reconstruction for given radiated electromagnetic fields. IEEE transactions on antennas and propagation. 2009;58(2):432–439.

[3] Kord A, Sounas DL, Alù A. Active microwave cloaking using parity-time-symmetric satellites. Physical Review Applied. 2018;10(5):054040.

[4] Chen A, Monticone F. Active scattering-cancellation cloaking: broadband invisibility and stability constraints. IEEE Transactions on Antennas and Propagation. 2019;68(3):1655–1664.

[5] Selvanayagam M, Eleftheriades GV. An active electromagnetic cloak using the equivalence principle. IEEE Antennas and Wireless Propagation Letters. 2012;11:1226–1229.

[6] Bisht MS, Srivastava KV. Controlling electromagnetic scattering of a cylindrical obstacle using concentric array of current sources. IEEE Transactions on Antennas and Propagation. 2020;68(12):8044–8052.

[7] Qian C, Zheng B, Shen Y, et al. Deep-learning-enabled self-adaptive microwave cloak without human intervention. Nature Photonics. 2020;14(6):383–390.

[8] Chen PY, Soric J, Alù A. Invisibility and cloaking based on scattering cancellation. Advanced Materials. 2012;24(44):OP281–OP304.

[9] Selvanayagam M, Eleftheriades GV. Experimental demonstration of active electromagnetic cloaking. Physical review X. 2013;3(4):041011.

[10] Sengupta S, Council H, Jackson DR, et al. Active radar cross section reduction of an object using microstrip antennas. Radio Science. 2020;55(2):1–20.

[11] Ang P, Eleftheriades GV. Active cloaking of a non-uniform scatterer. Scientific reports. 2020;10(1):1–11.

[12] Lopéz YA, Andrés FLH, Pino MR, et al. An improved super-resolution source reconstruction method. IEEE Transactions on Instrumentation and Measurement. 2009; 58(11):3855–3866.

[13] Quijano JLA, Vecchi G. Improved-accuracy source reconstruction on arbitrary 3-d surfaces. IEEE Antennas and Wireless Propagation Letters. 2009;8:1046–1049.

[14] Yao HM, Sha WE, Jiang LJ. Applying convolutional neural networks for the source reconstruction. Progress In Electromagnetics Research M. 2018;76:91–99.

[15] Foged L, Scialacqua L, Saccardi F, et al. Application of the dual-equation equivalent-current reconstruction to electrically large structures by fast multipole method enhancement [amta corner]. IEEE Antennas and Propagation Magazine. 2014;56(5):264–273.

[16] Persson K, Gustafsson M, Kristensson G, et al. Radome diagnostics—source reconstruction of phase objects with an equivalent currents approach. IEEE Transactions on Antennas and Propagation. 2014;62(4):2041–2051.
[17] Álvarez Y, Las-Heras F, Pino MR. Reconstruction of equivalent currents distribution over arbitrary three-dimensional surfaces based on integral equation algorithms. IEEE Transactions on Antennas and Propagation. 2007;55(12):3460–3468.
[18] Cai X, Geyi W. An optimization method for the synthesis of flat-top radiation patterns in the near-and far-field regions. IEEE Transactions on Antennas and Propagation. 2018; 67(2):980–987.
[19] Yu S, Liu H, Li L. Design of near-field focused metasurface for high-efficient wireless power transfer with multifocus characteristics. IEEE Transactions on Industrial Electronics. 2018;66(5):3993–4002.
[20] Ayestarán RG. Fast near-field multifocusing of antenna arrays including element coupling using neural networks. IEEE Antennas and Wireless Propagation Letters. 2018; 17(7):1233–1237.
[21] Iliopoulos I, Fuchs B, Sauleau R, et al. On the use of convex optimization for electromagnetic near-field shaping. In: 2017 11th European Conference on Antennas and Propagation (EUCAP); IEEE; 2017. p. 1013–1016.
[22] Ayestarán RG, León G, Pino MR, et al. Wireless power transfer through simultaneous near-field focusing and far-field synthesis. IEEE Transactions on Antennas and Propagation. 2019;67(8):5623–5633.
[23] Nepa P, Buffi A. Near-field-focused microwave antennas: Near-field shaping and implementation. IEEE Antennas and Propagation Magazine. 2017;59(3):42–53.
[24] Iliopoulos I, Fuchs B, Sauleau R, et al. Scalar near-field focusing in lossy media. In: 2017 International Conference on Electromagnetics in Advanced Applications (ICEAA); IEEE; 2017. p. 718–721.
[25] Wu JW, Wu RY, Bo XC, et al. Synthesis algorithm for near-field power pattern control and its experimental verification via metasurfaces. IEEE Transactions on Antennas and Propagation. 2018;67(2):1073–1083.
[26] Clauzier S, Mikki SM, Antar YM. Design of near-field synthesis arrays through global optimization. IEEE Transactions on Antennas and Propagation. 2014;63(1):151–165.
[27] Egarguin NJA, Jackson DR, Onofrei D, et al. Adaptive beamforming using scattering from a drone swarm. In: 2020 IEEE Texas Symposium on Wireless and Microwave Circuits and Systems (WMCS); 2020. p. 1–6.
[28] Brown T, Narendra C, Vahabzadeh Y, et al. On the use of electromagnetic inversion for metasurface design. IEEE Transactions on Antennas and Propagation. 2019;68(3):1812–1824.
[29] Huang C, Zhang C, Yang J, et al. Reconfigurable metasurface for multifunctional control of electromagnetic waves. Advanced Optical Materials. 2017;5(22):1700485.
[30] Boardman A, Alberucci A, Assanto G, et al. Waves in hyperbolic and double negative metamaterials including rogues and solitons. Nanotechnology. 2017;28(44):444001.
[31] Kurilkina SN, Petrov NS, Zimin AB, et al. Special inhomogeneous electromagnetic waves in hyperbolic metamaterials. Journal of Optics. 2017 nov;19(12):125102. Available from: https://dx.doi.org/10.1088/2040-8986/aa945c.
[32] Chen J, Hu S, Zhu S, et al. Metamaterials: From fundamental physics to intelligent design. Interdisciplinary Materials. 2022 07;2.
[33] Yin X, Zhu H, Guo H, et al. Hyperbolic metamaterial devices for wavefront manipulation. Laser & Photonics Reviews. 2018;13.
[34] Desouky M, Mahmoud A, Swillam M. Tunable mid ir focusing in inas based semiconductor hyperbolic metamaterial. Sci Rep. 2017;7.
[35] Lee S, Baek S, Kim T, et al. Mmetamaterials for enhanced optical responses and their application to active control of terahertz waves. Adv Mater. 2020;32(35).
[36] Abdelraouf O, Wang Z, Liu H, et al. Recent advances in tunable metasurfaces: Materials, design, and applications. ACS Nano. 2022;16(9):13339.

[37] Marengo EA, Devaney AJ. The inverse source problem of electromagnetics: Linear inversion formulation and minimum energy solution. IEEE Transactions on Antennas and Propagation. 1999;47(2):410–412.
[38] Egarguin NJA, Onofrei D, Qi C, et al. Active manipulation of helmholtz scalar fields in an ocean of two homogeneous layers of constant depth. Inverse Problems in Science and Engineering. 2021;:1–25.
[39] Qi C, Egarguin NJA, Onofrei D, et al. Feasibility analysis for active near/far field acoustic pattern synthesis in free space and shallow water environments. Acta Acustica. 2021;5:39.
[40] Egarguin NJA, Onofrei D, Qi C, et al. Active manipulation of helmholtz scalar fields: near-field synthesis with directional far-field control. Inverse Problems. 2020;36(9):095005.
[41] Onofrei D. Active manipulation of fields modeled by the helmholtz equation. Journal Of Integral Equations and Applications. 2014;26(4):553–572.
[42] Egarguin NJA, Onofrei D, Platt E. Sensitivity analysis for the active manipulation of helmholtz fields in 3d. Inverse Problems in Science and Engineering. 2020;28(3):314–339.
[43] Onofrei D, Platt E. On the synthesis of acoustic sources with controllable near fields. Wave Motion. 2018;77:12–27.
[44] Zeng S, Egarguin NJA, Onofrei D, et al. Active control of electromagnetic waves in layered media using a current source. In: 2020 IEEE Texas Symposium on Wireless and Microwave Circuits and Systems (WMCS); IEEE; 2020. p. 1–6.
[45] Onofrei D, Platt E, Egarguin NJA. Active manipulation of exterior electromagnetic fields by using surface sources. Quarterly of Applied Mathematics. 2020;78(4):641–670.
[46] Merzlikin AM, Puzko RS. Homogenization of maxwell's equations in a layered system beyond the static approximation. Scientific Reports. 2020;10(1):15783.
[47] Angell TS, Kirsch A. Optimization methods in electromagnetic radiation. Springer Science & Business Media; 2004.
[48] Qi C, Egarguin NJA, Zeng S, et al. Sensitivity analysis for active electromagnetic field manipulation in free space. Applied Mathematics in Science and Engineering. 2022;30(1):661–687. Available from: https://doi.org/10.1080/27690911.2022.2118270.
[49] Epstein CL, Greengard L. Debye sources and the numerical solution of the time harmonic maxwell equations. Communications on Pure and Applied Mathematics. 2010;63(4):413–463. Available from: https://onlinelibrary.wiley.com/doi/abs/10.1002/cpa.20313.
[50] Xiong XYZ, Sha WEI, Jun Jiang L. Helmholtz decomposition based on integral equation method for electromagnetic analysis. Microwave and Optical Technology Letters. 2014;56(8):1838–1843. Available from: https://onlinelibrary.wiley.com/doi/abs/10.1002/mop.28454.
[51] O'Neil M. A generalized debye source approach to electromagnetic scattering in layered media. Journal of Mathematical Physics. 2014;55(1):012901.
[52] Fu X, Li J, Jiang LJ, et al. Generalized debye sources-based efie solver on subdivision surfaces. IEEE Transactions on Antennas and Propagation. 2017;65(10):5376–5386.
[53] Epstein CL, Rachh M. Debye source representations for type-i superconductors, i: The static type i case. Journal of Computational Physics. 2022;452:110892. Available from: https://www.sciencedirect.com/science/article/pii/S0021999121007877.
[54] Michalski KA, Mosig JR. Multilayered media green's functions in integral equation formulations. IEEE Transactions on Antennas and Propagation. 1997;45(3):508–519.
[55] Li D, Wilton DR, Jackson DR, et al. Efficient computation of green's functions for lossy uniaxial anisotropic layered media. Radio Science. 2019;54(3):196–214.
[56] Aksun M, Dural G. Clarification of issues on the closed-form green's functions in stratified media. IEEE Transactions on Antennas and Propagation. 2005;53(11):3644–3653.
[57] Li D, Wilton DR, Jackson DR. Recent advances in evaluating green's functions for multilayered media and half-space problems. In: 2017 Computing and Electromagnetics International Workshop (CEM); IEEE; 2017. p. 1–2.
[58] Simsek E, Liu QH, Wei B. Singularity subtraction for evaluation of green's functions for multilayer media. IEEE transactions on microwave theory and techniques. 2006;54(1):216–225.

[59] Michalski KA. Extrapolation methods for sommerfeld integral tails. IEEE Transactions on Antennas and Propagation. 1998;46(10):1405–1418.
[60] Mosig J. The weighted averages algorithm revisited. IEEE Transactions on Antennas and Propagation. 2012;60(4):2011–2018.
[61] Rao S, Wilton D, Glisson A. Electromagnetic scattering by surfaces of arbitrary shape. IEEE Transactions on antennas and propagation. 1982;30(3):409–418.
[62] Mueller JL, Siltanen S. Linear and nonlinear inverse problems with practical applications. SIAM; 2012.
[63] Bonesky T. Morozov's discrepancy principle and tikhonov-type functionals. Inverse Problems. 2008;25(1):015015.

Appendix A. Dyadic Green's function in spatial domain

Taking the inverse 2-D Fourier transform, the spectral-domain Green's function can be converted back to the spatial domain. In (11), the evaluation of $\boldsymbol{\mathcal{G}}^{EJ}$ involves double infinite integral, which can be computationally intensive when the number of observation points is large. To accelerate the computation of (11), the Hankel transform is applied to reduce the double infinite integral into a single semi-infinite integral. The general Hankel transform is written as

$$\begin{aligned} F(\boldsymbol{\rho}-\boldsymbol{\rho}', z, z') &= \mathcal{S}_n\{\tilde{F}(k_\rho, z, z')\} \\ &= \frac{1}{2\pi}\int_0^\infty \tilde{F}(\mathbf{k}_\rho, z, z') J_n(k_\rho|\boldsymbol{\rho}-\boldsymbol{\rho}'|) k_\rho dk_\rho, \end{aligned} \tag{A1}$$

where the integral operator $\mathcal{S}_n\{\cdot\}$ is called the generalized Sommerfeld integral (SI). J_n is the Bessel function of the first kind of order n with $n = 0, 1, 2$. $\boldsymbol{\rho}$ and $\boldsymbol{\rho}'$ respectively denote the transverse projection of the observation point $\mathbf{r}$ and source point $\mathbf{r}'$ in xy-plane.

Therefore, the dyadic Green's function can be expressed with respect to 16 SIs,

$$\mathcal{G}^{EJ}(\boldsymbol{\rho}-\boldsymbol{\rho}', z, z') = \begin{bmatrix} \frac{-\mathrm{I}_1+\cos(2\gamma)\mathrm{I}_{13}}{2} & \frac{\sin(2\gamma)\mathrm{I}_{13}}{2} & \frac{\cos(\gamma)\mathrm{I}_7}{j\omega\varepsilon_0\varepsilon_z'} \\ \frac{\sin(2\gamma)\mathrm{I}_{13}}{2} & \frac{-\mathrm{I}_1-\cos(2\gamma)\mathrm{I}_{13}}{2} & \frac{\sin(\gamma)\mathrm{I}_7}{j\omega\varepsilon_0\varepsilon_z'} \\ \frac{\cos(\gamma)\mathrm{I}_{12}}{j\omega\varepsilon_0\varepsilon_z} & \frac{\sin(\gamma)\mathrm{I}_{12}}{j\omega\varepsilon_0\varepsilon_z} & \frac{\frac{\mathrm{I}_5}{j\omega\varepsilon_0\varepsilon_z}-\delta(\mathbf{r}'-\mathbf{r})}{j\omega\varepsilon_0\varepsilon_z'} \end{bmatrix} \tag{A2}$$

$$\mathcal{G}^{EM}(\boldsymbol{\rho}-\boldsymbol{\rho}', z, z') = \begin{bmatrix} \frac{-\sin(2\gamma)\mathrm{I}_{15}}{2} & \frac{-\mathrm{I}_3+\cos(2\gamma)\mathrm{I}_{15}}{2} & \frac{\sin(\gamma)\mathrm{I}_9}{j\omega\mu_0\mu_z'} \\ \frac{\mathrm{I}_3+\cos(2\gamma)\mathrm{I}_{15}}{2} & \frac{\sin(2\gamma)\mathrm{I}_{15}}{2} & \frac{\cos(\gamma)\mathrm{I}_9}{j\omega\mu_0\mu_z'} \\ \frac{-\sin(\gamma)\mathrm{I}_{10}}{j\omega\varepsilon_0\varepsilon_z} & \frac{\cos(\gamma)\mathrm{I}_{10}}{j\omega\varepsilon_0\varepsilon_z} & 0 \end{bmatrix} \tag{A3}$$

$$\mathcal{G}^{HJ}(\boldsymbol{\rho}-\boldsymbol{\rho}', z, z') = \begin{bmatrix} \frac{\sin(2\gamma)\mathrm{I}_{16}}{2} & \frac{\mathrm{I}_4-\cos(2\gamma)\mathrm{I}_{16}}{2} & \frac{-\sin(\gamma)\mathrm{I}_{10}}{j\omega\varepsilon_0\varepsilon_z'} \\ \frac{-\mathrm{I}_4-\cos(2\gamma)\mathrm{I}_{16}}{2} & \frac{-\sin(2\gamma)\mathrm{I}_{16}}{2} & \frac{\cos(\gamma)\mathrm{I}_{10}}{j\omega\varepsilon_0\varepsilon_z'} \\ \frac{\sin(\gamma)\mathrm{I}_9}{j\omega\mu_0\mu_z} & \frac{-\cos(\gamma)\mathrm{I}_9}{j\omega\mu_0\mu_z} & 0 \end{bmatrix} \tag{A4}$$

$$\mathcal{G}^{HM}(\boldsymbol{\rho}-\boldsymbol{\rho}',z,z') = \begin{bmatrix} \frac{-\mathrm{I}_2+\cos(2\gamma)\mathrm{I}_{14}}{2} & \frac{\sin(2\gamma)\mathrm{I}_{14}}{2} & \frac{\cos(\gamma)\mathrm{I}_8}{j\omega\mu_0\mu_z'} \\ \frac{\sin(2\gamma)\mathrm{I}_{14}}{2} & \frac{-\mathrm{I}_2-\cos(2\gamma)\mathrm{I}_{14}}{2} & \frac{\sin(\gamma)\mathrm{I}_8}{j\omega\mu_0\mu_z'} \\ \frac{\cos(\gamma)\mathrm{I}_{11}}{j\omega\mu_0\mu_z} & \frac{\sin(\gamma)\mathrm{I}_{11}}{j\omega\mu_0\mu_z} & \frac{\frac{\mathrm{I}_6}{j\omega\mu_0\mu_z}-\delta(\mathbf{r}'-\mathbf{r})}{j\omega\mu_0\mu_z'} \end{bmatrix} \tag{A5}$$

where cosine and sine functions in (A2)-(A5) are defined as

$$\begin{aligned} \cos(\gamma) &= \frac{x-x'}{|\boldsymbol{\rho}-\boldsymbol{\rho}'|} \\ \sin(\gamma) &= \frac{y-y'}{|\boldsymbol{\rho}-\boldsymbol{\rho}'|} \\ \cos(2\gamma) &= \frac{(x-x')^2-(y-y')^2}{|\boldsymbol{\rho}-\boldsymbol{\rho}'|^2} \\ \sin(2\gamma) &= 2\frac{(x-x')(y-y')}{|\boldsymbol{\rho}-\boldsymbol{\rho}'|^2} \end{aligned} \tag{A6}$$

$\mathrm{I}_i, i = 1, 2, \ldots, 16$ denote 16 independent SIs. The discussion of the SIs is beyond the scope of this article. More details can be referred to [55].